



Dual-site catalysts featuring platinum-group-metal atoms on copper shapes boost hydrocarbon formations in electrocatalytic CO₂ reduction

Received: 28 July 2022

Accepted: 16 May 2023

Published online: 27 May 2023

Check for updates

Manjeet Chhetri^{1,7}, Mingyu Wan^{2,7}, Zehua Jin^{1,7}, John Yeager¹, Case Sandor¹, Conner Rapp¹, Hui Wang³, Sungsik Lee⁴, Cameron J. Bodenschatz⁵, Michael J. Zachman⁶, Fanglin Che²✉ & Ming Yang¹✉

Copper-based catalyst is uniquely positioned to catalyze the hydrocarbon formations through electrochemical CO₂ reduction. The catalyst design freedom is limited for alloying copper with H-affinitive elements represented by platinum group metals because the latter would easily drive the hydrogen evolution reaction to override CO₂ reduction. We report an adept design of anchoring atomically dispersed platinum group metal species on both polycrystalline and shape-controlled Cu catalysts, which now promote targeted CO₂ reduction reaction while frustrating the undesired hydrogen evolution reaction. Notably, alloys with similar metal formulations but comprising small platinum or palladium clusters would fail this objective. With an appreciable amount of CO-Pd₁ moieties on copper surfaces, facile CO* hydrogenation to CHO* or CO-CHO* coupling is now viable as one of the main pathways on Cu(111) or Cu(100) to selectively produce CH₄ or C₂H₄ through Pd-Cu dual-site pathways. The work broadens copper alloying choices for CO₂ reduction in aqueous phases.

Among the catalytic reactions that can hydrogenate CO₂ into energy-intensive hydrocarbon molecules (HCs), the electrocatalytic CO₂ reduction reaction (CO₂RR) featuring CO₂ hydrogenation without producing H₂ gas in any prior steps is of particular interest. While there are ample choices of elements to catalyze CO₂RR into CO and formate molecules¹, copper (Cu) is the demonstrated element that can effectively catalyze the HCs formation (especially C₂₊) owing to its optimal binding energies for both hydrogen (ΔE_{H^*}) and carbonyl species (ΔE_{CO^*})^{2,3}, the ubiquitous intermediate during CO₂RR. Copper, therefore, serves as a unique catalytic metal to not only enable the circular

carbon economy on earth but to extend human life beyond earth's orbit through in situ utilization of the in-space CO₂ to make methane as fuel or ethylene as building block molecules.

Metal alloying is a broadly employed strategy to accelerate the CO₂RR while reasonably suppressing the competitive hydrogen evolution reaction (HER)^{4,5}. Metals such as Ag, Au, Pb, and Sn that are either in the same group or to the right of Cu in the periodic table have been extensively studied⁶. These metals, with a typical positive H* binding energy (>0.5 eV), are the well-accepted desired alloying choices with copper due to their unfavorable energetics toward the

¹Department of Chemical and Biomolecular Engineering, Clemson University, Clemson, SC, USA. ²Department of Chemical Engineering, University of Massachusetts Lowell, Lowell, MA, USA. ³Institute for New Energy Materials and Low Carbon Technology, Tianjin University of Technology, Tianjin, China. ⁴X-ray Science Division, Argonne National Laboratory, Lemont, IL, USA. ⁵Environmental Effects and Coatings Branch, NASA John H. Glenn Research Center, Cleveland, OH, USA. ⁶Center for Nanophase Materials Sciences, Oak Ridge National Laboratory, Oak Ridge, TN, USA. ⁷These authors contributed equally: Manjeet Chhetri, Mingyu Wan, Zehua Jin. ✉e-mail: Fanglin_Che@uml.edu; myang3@clemson.edu

HER³. However, limitations are inevitable on the product side - these alloyed metals naturally render weakened ΔE_{CO^*} and thus limit the main products to either formate or CO molecules^{7–10}, defeating the initial purpose of using Cu as a catalytic metal to enable deeper hydrogenation of CO₂.

If HER is never a concern, the above limitations can be straightforwardly addressed by incorporating platinum group metals (PGMs) residing on the left side of Cu in the periodic table, as the PGMs would provide substantial binding energy for CO^{*}. However, many studies suggest that incorporating PGM components, such as nanoparticles and clusters, into Cu catalysts often results in penalties for enhanced HER along with improved conversion rates of carbon-based products, if any^{11–15}. While it is indisputable that populating the catalyst surface with CO^{*} reduces the amount of H^{*} and the chance for subsequent H-H coupling to produce hydrogen gas^{16–20}, HER is still, kinetically, a considerably faster reaction on many PGM moieties as compared to CO₂RR (2e⁻ transfer vs. multi-electron transfer reaction)²¹. This pitfall was addressed in a series of recent works^{22–24} at a device level by incorporating catalysts on PTFE-based gas diffusion electrode (GDE) or catalyst-PFSA heterojunction arrangement as the electrode (by decoupling the gas-ion-electron transport process) to mitigate the HER tendency. In this work, from the perspective of designing the PGM-Cu catalytic center itself, we set out to find an alternative structure of the PGM-Cu interface that can favor CO₂ hydrogenation to HCs through Cu but intrinsically limit HER. To unfold this possibility, we propose that two critical aspects of nanocatalyst design shall be satisfied simultaneously: (1) the PGM species anchored on the Cu host must be structured differently as opposed to extended PGM surfaces known to promote HER; (2) the PGM species as identified in aspect#1, must utilize the nearby Cu surfaces to render the enrichment of CO^{*} for further hydrogenation.

Herein, we report the design, synthesis, and characterizations of Pd₁Cu (as the primary research target) and Pt₁Cu single-atom alloys (SAAs) nanocatalysts for facile CH₄ and C₂H₄ formation through CO₂RR. With a trace amount of PGMs acting as the CO^{*} promoting sites and the preserved CO₂ hydrogenation chemistry on Cu, promising results were made from the SAAs. Through shape-controlled catalyst synthesis, in-situ reaction studies, and DFT calculations, we demonstrate how PGM₁Cu SAAs, as dual-site catalysts, enhance CO₂RR performance without

disrupting the HC formation capacity created by their parent Cu catalysts.

Results

Design of PGM₁-Cu SAAs materials

To begin, we performed the work based on polycrystalline Cu nanoparticles (NPs) to reflect the general relevance of the work and then we developed specific shape-controlled catalysts for reaction mechanistic-oriented studies. We used galvanic displacement (GD) to synthesize SAAs using M²⁺ salts (M = Pd²⁺, Pt²⁺) to replace the elemental Cu, referred to as Pd₁Cu SAA and Pt₁Cu SAA. We adopted a modified wet chemical method^{25,26} using ascorbic acid as a reducing agent and antioxidant for Cu NPs, instead of using commercial Cu directly. This approach minimizes the presence of Cu₂O on the parent Cu surface, as found in commercial Cu (Supplementary Fig. S1a and associated discussion), thus circumventing the potential negative effects of Cu₂O on the synthesis of SAA and the resulting catalytic activity. By accurately controlling the concentration of the PGM salts and the time of exchange during the GD synthesis (to be discussed soon), we made a series of SAA catalysts favoring the HCs yields over the HER side reaction during the CO₂RR. In this work, we mainly discuss the characterizations and CO₂RR activity of Pd₁Cu and highlight about Pt₁Cu when appropriate for discussion.

To begin the investigation, field emission scanning electron microscopy (FESEM) and high-resolution transmission electron microscopy (HR-TEM, insert) in Fig. 1a shows a polycrystalline nature of a generic Cu-based catalyst ranging from 50–150 nm (Supplementary Fig. S1b). Next, energy dispersive spectroscopy (EDS) elemental mapping, as shown in Fig. 1a, indicates the presence of Pd in a highly dispersed state, and its dilute concentration with the Cu host is 0.9 wt.% according to ICP analyses (Supplementary Table S1). Further, the Pd moieties were identified as single-atom species on the lattice of Cu by aberration-corrected high angle annular dark-field scanning transmission electron microscopy (HAADF-STEM) (Fig. 1b and Supplementary Fig. S2). We analyzed the Pd K-edge of the Pd₁Cu SAA as-prepared/post-reaction catalysts by the extended X-ray absorption fine structure (EXAFS). As evident from Fig. 1c and Supplementary Table S2, the Pd atoms in these Pd₁Cu SAA samples are stabilized through the Pd-Cu coordination in the first shell at a radial distance of ~2.60 Å. The possible contribution of Pd-Pd coordination near 2.74 Å is minimal in these

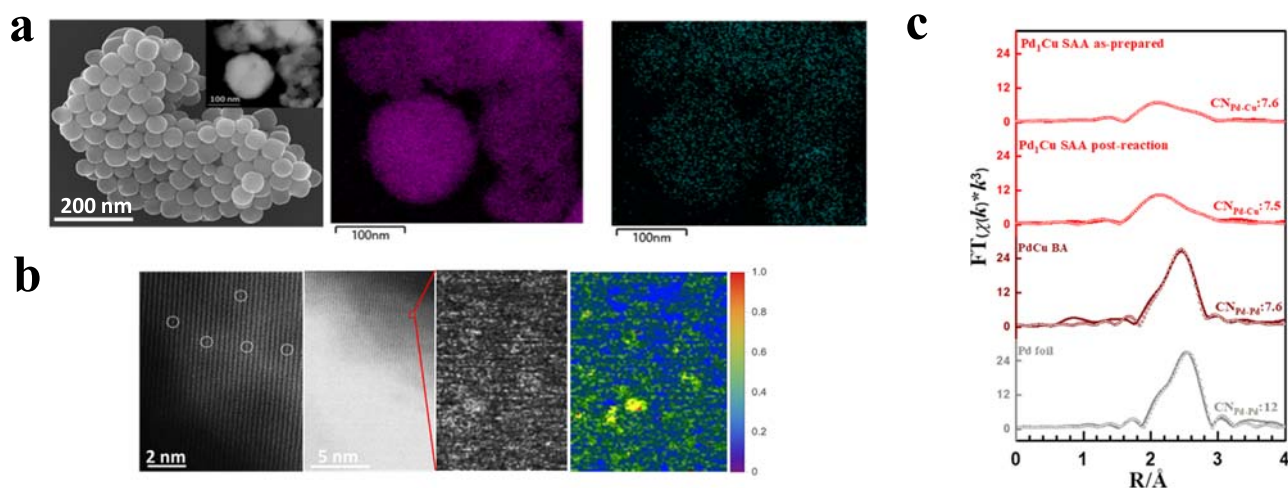


Fig. 1 | Morphology and structure analyses of polycrystalline PGM-Cu SAAs. **a** FESEM image of the polycrystalline Cu catalyst and the inset shows the Pd₁Cu SAA along with its corresponding EDS elemental map (right) showing the atomic distribution of Pd on the parent Cu surface. **b** Aberration-corrected HAADF-STEM images for the Pd₁Cu SAA (left). The circles highlight the single-atom Pd. Enlarged

and colorized intensity map of the highlighted red square region showing isolated Pd atoms (center): yellow-red regions in the color contour represent Pd atomic dispersion and blue represents Cu surface (right). **c** Pd K-edge EXAFS (shaded lines) and the curve-fit (points) for Pd₁Cu SAA as-prepared, Pd₁Cu SAA post-reaction, PdCu BA, and Pd foil is shown in *R*-space.

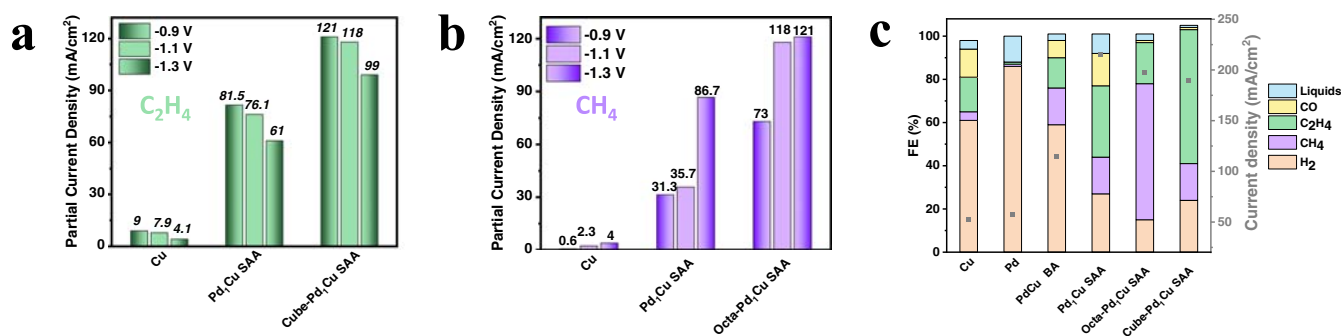


Fig. 2 | Electrochemical CO₂ reduction activity comparison. The partial current density of **a** C₂H₄ and **b** CH₄ at different voltages (*vs.* RHE) for polycrystalline Cu, polycrystalline Pd₁Cu SAA, and shape-controlled Pd₁Cu SAAs. **c** Comparison of CO₂ reduction FE% and current densities of Pd₁Cu SAAs and their key counterparts. FE%

analysis was performed by running an amperometric *i-t* curve at -1.1 V *vs.* RHE and quantifying the products over 30 min. The catalyst loading on the GDE was maintained at about 220 $\mu\text{g}/\text{cm}^2$ for these tests.

SAA as-prepared and post-reaction samples, indicating the Pd atoms are isolated by the surrounding Cu atoms to avoid aggregations even after the CO₂RR. These first-shell Pd-Cu and Pd-Pd distances agree well with the previous studies^{27–29}. In addition, the consistent Pd-Cu coordination around 7.5 (CN=12 is usually for bulk alloys) in both as-prepared and post-reaction SAA catalysts suggests that single-atom Pd species reside on the catalyst surface and the local coordination environment for the Pd experiences minimal change after the reaction, indicating the promising stability of the SAA structure.

To compare with the SAAs made by the GD method, we also synthesized dilute PdCu bimetallic alloys (BAs) through the conventional coprecipitation approach by using a dilute amount of Pd precursor and NaBH₄ as a reducing agent. The NaBH₄-induced reduction leads to preferred Pd-Pd bond formation with BA structure resembling nanoparticulate or cluster forms. In contrast to the single-atom Pd nature in the Pd₁Cu SAA catalyst, we observe a CN_{Pd-Pd} of 7.6 for the PdCu BA, suggesting the presence of small Pd nanoclusters³⁰ in the BA catalyst as our reference sample designs intended (Fig. 1c and Supplementary Table S2). The ICP data (Supplementary Table S1) and CO₂RR reactivity screening results (Supplementary Fig. S3a) reveal that, even with similar or lower concentrations of Pd, the incorporated Pd in the BA catalysts fails to deliver any significantly improved HCs formation or suppressed HER. We observed similar behaviors upon characterizing the Pt₁Cu system (Supplementary Tables S1 and Figs. S3b & S4). These results indicate that a general formulation of dilute PGMs in Cu is not a guarantee for the improved catalytic performance to be discussed shortly in this report.

Enhanced CO₂RR to HCs and Reduced HER by PGM₁-Cu SAAs

We tested the CO₂RR activity in a flow-cell electrolyzer (3-compartment cell with 1cm² gas diffusion electrode (Supplementary Figs. S5 and S6) using CO₂-saturated 0.5 M KHCO₃ as electrolyte and CO₂ gas feed as the reactant). All the reported potentials are referenced to the reversible hydrogen electrode (RHE) unless specified otherwise. Among the key samples, there were negligible liquid products and a similar amount of gaseous CO formation (Supplementary Figs. S7 and S8 and Table S3). To begin with the conversion rate, at -0.9 V, the polycrystalline Pd₁Cu SAA exhibits multi-fold improved CH₄ and C₂H₄ partial current densities as compared to its parent polycrystalline Cu NPs (Fig. 2a, b). This improvement is dramatic in part because the catalyst loading on the GDE was maintained at about 220 $\mu\text{g}/\text{cm}^2$. When a much higher (1 mg/cm²) catalyst loading was used, the reactivity difference between the samples shrank to 2–3 times due to the more significant mass transfer limitations to the SAA samples. On the reaction selectivity, as compared to Cu NPs, the Pd₁Cu SAA shows significant improvement in HCs products (Supplementary Fig. S7 for itemized columns at -1.1 V). The Faradaic efficiency (FE) of CH₄

increases from 6 to 25% and the C₂H₄ from 16 to 33% from the Cu NPs to Pd₁Cu SAA. Notably, with an almost identical chemical formulation, the bimetallic alloy PdCu BA fails to deliver any similar improvement for CH₄ and C₂H₄ production in terms of FE and current densities when measured against the Pd₁Cu SAA. Worse, the creation of Pd-Pd, even in small clusters, in the PdCu BA sample leads to a doubled FE for HER. As expected, the HER becomes the single-dominant reaction in the case of Pd-only nanoparticles. By estimating the electrochemically active surface area (ECSA) that is proportional to the double-layer capacitance of the catalysts (Supplementary Fig. S9), we confirmed that the galvanic exchange preparation method does not improve the ECSA to give rise to the reactivity boost.

We have further made shape-controlled Cube Pd₁Cu SAA and Octahedral (Octa- in short) Pd₁Cu SAA to improve the admittedly mediocre performance of the initial polycrystalline catalysts in terms of partial current density and FE for CH₄ or C₂H₄ formation (Fig. 2 and Supplementary Fig. S3), and more importantly, to bridge to mechanistic studies in later sections of this report. Since Cu(100) faceted (Cube surface) and Cu(111) faceted (Octahedra surface) crystals yield C₂H₄ and CH₄ as major products³¹, respectively, we leveraged the Pd₁Cu SAA recipe to enhance the CO₂RR performance towards either CH₄ or C₂H₄ selectively. These shape-specific SAAs are stable with a partial current density of ca. 100 mA/cm² and FE > 50% for a reaction duration of over 300 min (Supplementary Fig. S10).

We observed a similar encouraging trend when adopting Pt besides Pd through the SAA strategy for reaction tests using 0.5 M KHCO₃ (Supplementary Figs. S3b, S8, S11). These Pd₁- and Pt₁-Cu SAAs rank among the highly promising PGM-containing catalysts for CO₂RR in making HCs (Supplementary Table S4 and Fig. S12a, b). Although the commercial Cu (particle size 40–60 nm, Sigma Aldrich) seems to be a better platform than our home-made Cu to achieve appreciable CH₄ and C₂H₄ formations, we were unable to use the commercial Cu as the starting material to produce the SAA catalyst, as discussed earlier (Supplementary Fig. S1a). Nevertheless, we benchmarked the Pd₁Cu SAA using the inferior homemade Cu with the advanced commercial Cu sample, and we are still able to confirm the enhanced activity from the SAA (Supplementary Fig. S13a). Besides the alloy catalytic chemistry, the surface pH increase at higher current densities may well be the external contributor toward the limited HER and enhanced HCs formation. Hence, we performed additional reaction studies for the Cu and Pd₁-Cu SAA catalysts with different electrolyte pHs (and estimated surface pHs) at the same ionic strength. While the higher pH indeed helps the reactions of interest, the Pd₁-Cu SAA catalysis is clearly the more significant contributor (Supplementary Fig. S13b and associated discussion).

We caution readers that the present work intends to improve the CO₂RR performance from the aspect of nanocatalyst engineering for

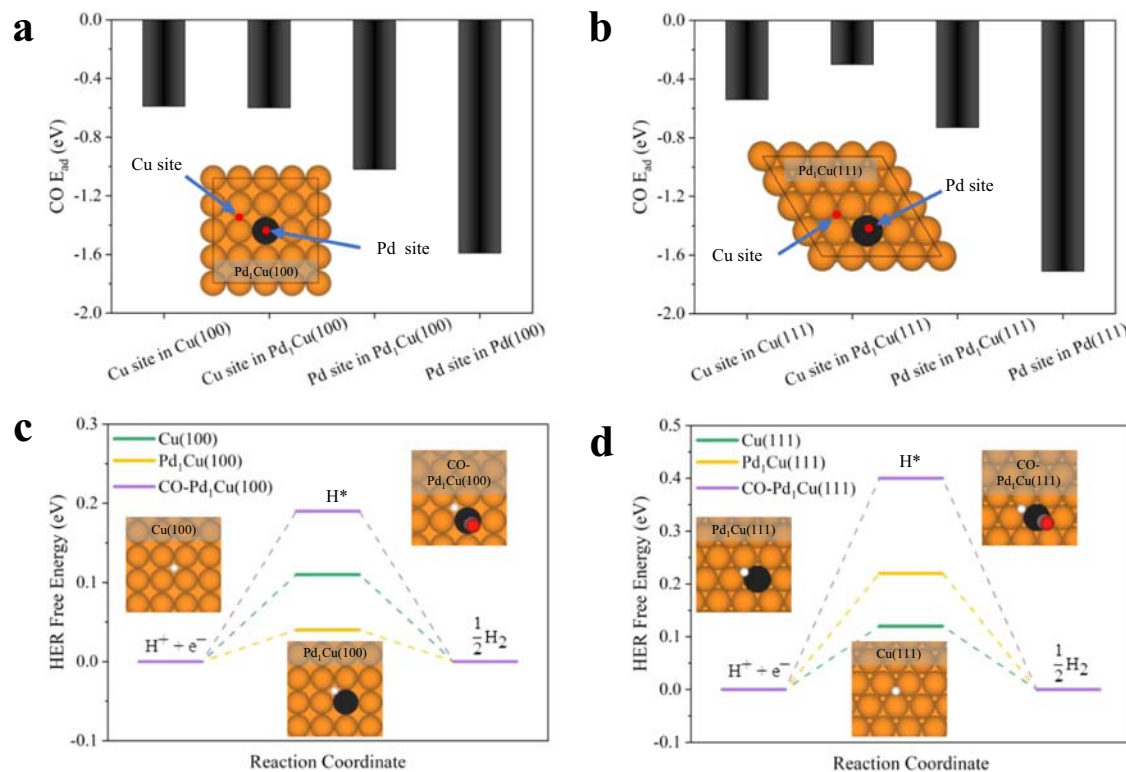


Fig. 3 | DFT calculations on the role of single-atom Pd in Pd₁Cu SAA on tuning the CO' adsorption and HER. **a, b** show the adsorption energy of CO' over (100) and (111) facets of bare Cu, Pd₁Cu, and bare Pd, respectively. The top views of Pd₁Cu(100) and (111) with their possible CO' adsorption sites (red) are inserted. **c, d** are the free energy diagram of HER over (100) and (111) facets of bare Cu, Pd₁Cu,

and Pd₁Cu with the presence of a CO molecule adsorption over the Pd site (CO-Pd₁Cu). The HER free energy was calculated under standard conditions. The configurations of H' on these three scenarios are inserted. Color code: Cu (orange), Pd (black), C (gray), O (red) and H (white).

mediocre metallic copper catalysts made in-house, so the reported activity boost shall not be regarded as the ultimate high performance for any Cu-based catalysts, especially at the device level. More detailed discussion on this matter can be found in the *Discussion* section. Additionally, the dramatic differences in the catalytic performances, as we observed, are not a result of the overall catalyst particle size changes, as indicated by the similar size of Cu NPs with or without displaced PGM shown in Fig. 1a and Supplementary Figs. S1a, S2, and S4. It has been previously reported that the difference in particle size influences the CO₂RR product selectivity^{32,33}. However, in our experiment, the influence of particle sizes with narrower distribution on reaction selectivity won't be explicitly reflected. The above results show that to steer CO₂RR towards more HCs without compromises for favoring HER simultaneously, it is beneficial to include PGM atoms in the catalysts but most likely only in the form of isolated PGM atoms.

Desired CO' and H' Interactions of PGM₁Cu SAA

We performed DFT calculations and examined the role of Pd₁Cu SAA interfacing with the ubiquitous CO₂RR early intermediates, namely CO' and H' on catalyst surfaces^{3,34,35} (for details of DFT calculations, see Methods, Supplementary Information, and Fig. S14). Pd₁Cu(100) and Pd₁Cu(111) surfaces were selected for DFT calculations. This is because the computational supercells of Pd₁Cu(111) and Pd₁Cu(100) matched reasonably well with the experimental shape-controlled samples in terms of averaged Pd-Cu distance (2.61 Å for Pd₁Cu(111), 2.66 Å for Pd₁Cu(100) in theory vs. -2.61 Å for Octa Pd₁Cu SAA and -2.65 Å on average for Cube-Pd₁Cu SAA in experimental, see Supplementary Table S2) and Pd-Cu coordination number (9 for Pd₁Cu(111), 8 for Pd₁Cu(100) in theory vs. -8.7 for Octa Pd₁Cu SAA and -7.6 on average for Cube-Pd₁Cu SAA in experimental, see Supplementary Table S2). For CO' over the Pd₁Cu(100) surface (Fig. 3a), we studied different

adsorption sites (Supplementary Table S5), including Cu site, Pd site and Pd-Cu interfacial sites. We found that CO' over the Pd_{top} site has the most favorable adsorption energy of -1.02 eV, which is stronger than that on Cu(100) of -0.59 eV but weaker than that on Pd(100) of -1.59 eV. The adsorption energy values indicate that the presence of the single-atom Pd could improve CO' adsorption significantly compared to the bare Cu(100). It is worth mentioning that the most favorable CO' adsorption energy on the Cu site of Pd₁Cu(100) is nearly the same as that of Cu(100). This means the single-atom Pd doesn't influence the CO' adsorption performance over the nearby Cu atoms. We obtained similar results for the Pd₁Cu(111) surface (Fig. 3b). Among all sites of Pd₁Cu(111) (Fig. 3 and Supplementary Table S6), CO' over the Pd_{top} site has the strongest CO' adsorption energy of -0.73 eV, which is larger than that on Cu(111) of -0.54 eV but weaker than that on Pd(111) of -1.71 eV. When CO' adsorbs over the Cu site of Pd₁Cu(111), its adsorption energy is slightly weaker than the pure Cu(111) surface by -0.2 eV. Thus, for a typical Pd₁Cu SAA, the Cu site behaves like pure Cu for CO' adsorption, and the Pd₁ site renders stable adsorption of CO'.

To probe the translational effect, we also performed the CO' adsorption on the Pt₁Cu SAA surfaces (Supplementary Fig. S15 and Tables S5-S6). The DFT results show that the Pt₁ site significantly strengthens the CO' adsorption, similar to the Pd₁ site. The most favorable adsorption sites of CO' are the Pt_{top} sites, with adsorption energies of -1.42 eV and -1.06 eV over Pt₁Cu(100) and Pt₁Cu(111) surfaces, respectively. The results suggest that the single-atom PGM (i.e., Pd, Pt) on the Cu matrix plays a similar role in strengthening the CO' adsorption and potentially achieving a higher CO' surface coverage than the pure Cu surfaces. To quantify the impact of the single-atom PGM on the binding and the surface coverage of CO, we calculated the adsorption free energy of adding CO one by one on Pd₁Cu(100) and Cu(100) surfaces (Supplementary Fig. S16). Our results indicate that

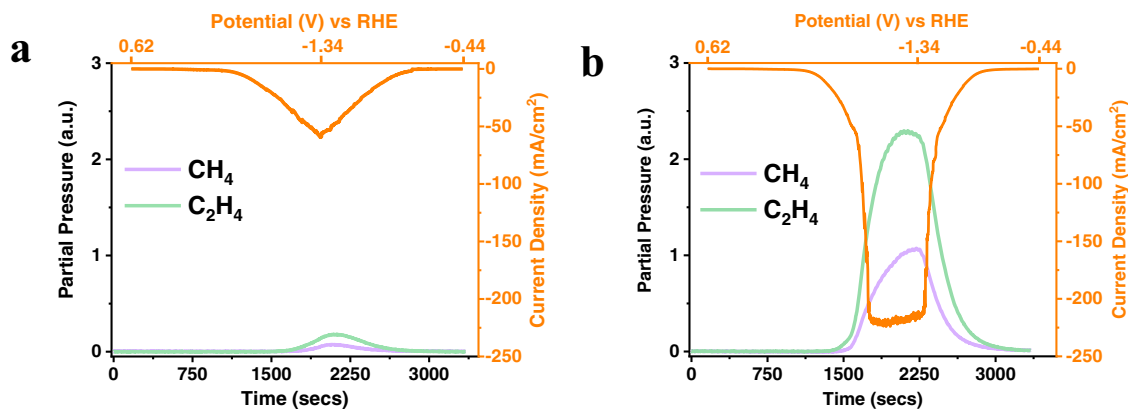


Fig. 4 | Real-time analysis of gaseous products as a function of scanning potential. Cyclic voltammograms and real-time hydrocarbon product distribution detected by mass spectrometer upon CO₂ reduction using **a** parent Cu NPs and **b** Pd₁Cu SAA. The potential was scanned at 1 mV/sec, and mass spectrometer data points were collected every 4 s providing the matching time interval of the online

analysis of products as a function of voltage. The measurement was started after reaching the steady-state condition. Potential is scanned from open-circuit voltage to -1.34 V (vs. RHE) and then reversed back to -0.44 V (vs. RHE). (a.u.: arbitrary units).

when CO adsorbed over the PGM of Cu-based SAA, the adsorption free energy of CO is significantly higher (-0.4 eV) than that of the pure Cu, and the PGM didn't change the adsorption free energies of other CO adsorbates over the Cu sites of SAAs. Thus, SAAs can potentially increase the CO surface coverage and the degree of the increment of the CO surface coverage depends on the densities of the PGM of SAAs. The overly strong binding of carbonyl species may inhibit the subsequent hydrogenation steps. Considering the dilute atomic dispersion of PGM on Cu surface, notorious CO poisoning is expected not to be an issue in our case. Toward this objective, we performed CO stripping experiments for Pt₁Cu SAA, PtCu BA, Cu-only, and Pt-only catalysts (Supplementary Fig. S17). We chose Pt over Pd for this study to correlate better the hydrogen underpotential deposition (H_{UPD}) and CO adsorption properties on the catalyst surface due to the distinguishable signals of Pt as compared to that of Pd for CO adsorption/desorption. The results suggest that the Pt₁Cu SAA catalyst, behaving almost like the Cu-only reference in this experiment, has remarkable anti-CO-poisoning capability when measured against the Pt-only and PtCu BA counterparts.

How does the PGM₁Cu SAA hold for HER activity? We investigated the role of the Pd site in Pd₁Cu by examining the free energy of HER. To construct the free energy diagram of HER, we considered two scenarios, including H⁺ over the clean Pd₁Cu SAA (Supplementary Tables S7 and S8) and H⁺ over the Pd₁Cu SAA with one pre-existing CO^{*} on the top site of Pd (Fig. 3c, d). The results show that when there is a pre-existing CO^{*} on the top site of Pd of the Pd₁Cu SAA, the free energies of HER over Pd₁Cu SAA are increased by 0.08 eV and 0.28 eV compared to Cu(100) and Cu(111) and thus, HER is suppressed. This finding is also translational to Pt₁Cu SAA (Supplementary Tables S7–S8). The free energy diagram for HER (Supplementary Fig. S15c, d) shows that when there is a pre-existing CO^{*} on the top site of Pt of the Pt₁Cu SAA, the free energies of HER over the Pt₁Cu(100) and Pt₁Cu(111) SAA increase by 0.20 eV and 0.42 eV compared to those over Cu(100) and Cu(111), respectively. Therefore, DFT results suggest that HER could be suppressed thermodynamically by PGM₁Cu SAA due to the lateral interaction raised by strong, co-adsorbed CO^{*} over the PGM top site. This is consistent with the previous theoretical studies that an improved CO^{*} coverage and a stronger CO^{*} adsorption energy could weaken H⁺ adsorption and reduce HER^{14–18}. Our theoretical results are also in agreement with our experimental findings that Pd₁Cu significantly suppresses the FE of HER as compared to the pure Cu catalyst under CO₂RR conditions. Indeed, in the event of non-CO₂RR reaction condition, as the DFT results suggested, the PGM₁Cu configurations may promote the HER compared with the parent Cu-only

surfaces, and our blank reaction test using Ar instead of CO₂ in the gaseous feed stream confirmed this prediction as well (Supplementary Figs. S7 and S8).

Mechanistic Interrogation of Pd₁Cu SAAs for CO₂RR

Figure 4 shows the evolution of products by slow voltage scanning from open-circuit voltage to -1.34 V and then back to -0.44 V through our online CV-Mass spectrometer setup. Compared with the parent Cu-only catalyst, we observe an earlier onset of CH₄ and C₂H₄ by scanning the potential in a more negative direction for the Pd₁Cu SAA catalyst, which drives the rapid increase in current density as the HCs formation becomes more significant. Similar phenomena can be observed on Pt₁Cu SAA catalyst, as shown in Supplementary Fig. S18. These results indicate that the PGMs enrich the catalyst surface with crucial reaction intermediates leading to facile reactions under the CO₂RR condition.

We benchmarked these findings by synthesizing Cu cubes exposing Cu(100) facet and Cu octahedra exposing Cu(111) facet (Fig. 5a–c) and alloying reaction-stable atomically dispersed Pd species on these Cu shapes (Fig. 5d for EXAFS, Supplementary Fig. S19 for elemental mapping). Since Cu(100) faceted (Cube surface) and Cu(111) faceted (octahedra surface) crystals yield C₂H₄ and CH₄ as major products, respectively³¹, we leveraged our Pd₁Cu SAA recipe to enhance the CO₂RR performance of these shape-controlled catalysts toward either CH₄ or C₂H₄ selectively (Supplementary Fig. S20). As discussed earlier, these shape-controlled Pd₁Cu SAAs are advantageous to the polycrystalline SAAs (Fig. 2c), and they rank among the highly promising PGM-containing catalysts for CO₂RR in making HCs (Supplementary Table S4 and S12a and S12b). With the help of the single-atom Pd, these shape-controlled Pd₁Cu SAAs also show enhanced FE and improved partial current density for targeted products than their parent Cu-only cube and octahedra samples (Supplementary Fig. S20). Perhaps the more exciting fundamental observation is that the Cube-Pd₁Cu SAA and Octa-Pd₁Cu SAA specifically enhances the CH₄ and C₂H₄ formation, respectively, without altering the intrinsic selectivity of their parent Cube-Cu and Octa-Cu samples (Fig. 5e). The observation of preserved Cu catalytic property after doping is unusual yet desired in CO₂RR research for HC formations, where the alloying strategy with various types of the second metal often leads to overhauls of reactivity and selectivity^{7–10}.

To probe the impact of the SAA on reaction pathways for CO₂RR by copper, we conducted the in-situ ATR-SEIRAS at -0.8 and -1.2 V for polycrystalline Cu NPs and Pd₁Cu SAA as the initial comparisons. Supplementary Fig. S21 and Table S9 show the time evolution of the

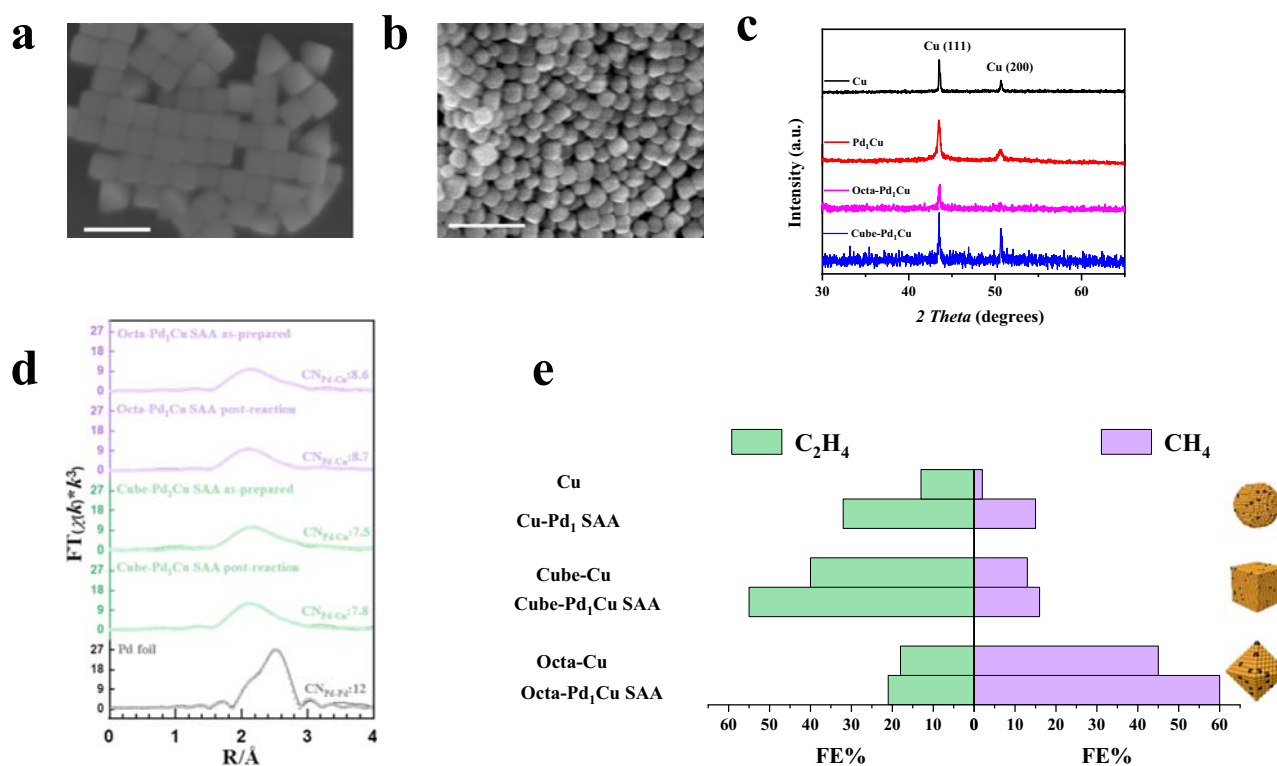


Fig. 5 | Effect of Pd on Cu for product distribution during CO₂ reduction. SEM image of **a** Cube-Cu and **b** Octa-Cu. The scale bar is 200 nm. **c** Powder X-Ray diffraction patterns of polycrystalline and shape-controlled Cu nanoparticles and Pd₁Cu SAAs. (a.u.: arbitrary units). **d** Pd K-edge EXAFS (shadowed lines) and the

curve-fit (points) for Octa-Pd₁Cu SAA as-prepared, Octa-Pd₁Cu SAA post-reaction, Cube-Pd₁Cu SAA as-prepared, Cube-Pd₁Cu SAA post-reaction, and Pd foil are shown in *R*-space. The data are *k*³-weighted and not phase-corrected. **e** The FE distribution of CH₄ and C₂H₄ obtained using Cu and Pd₁Cu SAAs (at -1.1 V *vs.* RHE).

absorbance peaks mainly between 1000 to 1800 cm⁻¹, where the peak assignments were based on the collective information from recent literature^{36–38}. While the polycrystalline Cu NPs lagged the polycrystalline Pd₁Cu SAA in terms of absorbance peak evolutions as a function of applied voltage and reaction time, both samples exhibit similar patterns in terms of wavenumbers in the IR spectra, suggesting the reaction pathway for the catalysts could be similar. Speaking of the promotion effect, SAA helps in decreasing the overpotential for the formation of a variety of intermediates. At -0.8V, the onset of CO₂ reduction is observed over polycrystalline SAA as indicated by the evolution of peaks for COOH^{*}, which is one of the early intermediates for CO₂RR toward CO₂ hydrogenation, but such species cannot be clearly detected until -1.2V over Cu NPs. Similarly, the formations of CHO^{*}, OCCHO^{*}, OCCO^{*}, and OCH₂^{*}, indicative of C₂H₄ and CH₄ formations and albeit appearing as a mixed package in the spectra, have already proceeded over SAA at -0.8V, whereas -1.2V would be required for the polycrystalline Cu NPs.

A similar trend in the ATR-SEIRAS can be tracked in the shape-controlled Cu and SAA catalysts as shown in Fig. 6, indicating that the introduced single-atom Pd on shape-controlled Cu will not necessarily create completely new reaction pathways but promote the CO₂RR reaction based on the parent copper. Importantly, the ATR-SEIRAS studies on these shape-controlled samples allow us to gain better resolution to distinguish the otherwise mixed CH₄ and C₂H₄ formation routes displayed by the polycrystalline samples. As the reaction test result suggested (Fig. 5e and Supplementary Fig. S20), Octa-Cu and Octa-Pd₁Cu SAA catalysts favorably catalyze the CH₄ formation in CO₂RR. In the corresponding ATR-SEIRAS spectra of these two Octa-series samples, an OCH₂^{*} characteristic peak can be detected around 1250 cm⁻¹, and this is one of the main intermediates for CH₄

production. In the meantime, it is hard to detect C-C coupling intermediates such as OCCHO^{*} at 1580 cm⁻¹ and OCCO^{*} at 1560 cm⁻¹ in these catalysts. Differently, Cube Cu and Cube Pd₁Cu SAA catalyze the C₂H₄ formation favorably (Fig. 5e and Supplementary Fig. S20). In the corresponding ATR-SEIRAS spectra of these Cube-series samples, OCCHO^{*} (more prominent) and OCCO^{*} intermediates from C-C coupling can be detected at 1580 and 1560 cm⁻¹, respectively. As the precursor intermediates to these C-C coupling intermediates, CHO^{*} at 1230 cm⁻¹ and COH^{*} at 1160 cm⁻¹ can also be detected. In comparison, OCCHO^{*} and its precursor CHO^{*} have more noticeable abundance compared to OCCO^{*} and COH^{*}, indicating OCCHO^{*} is a more prevalent C-C coupling in our catalysts and testing conditions. As an additional minor point, the Cube-series samples display a shoulder peak at slightly higher wavenumbers than the designated OCH₂^{*} for CH₄ formation in the Octa-series samples, and we cautiously attribute this minor shoulder peak to OCH₂^{*}-related C₂ oxygenate radicals toward ethylene formation³⁹.

Our DFT results agree with the above experimental observations. When CO^{*} hydrogenates through a surface H^{*} and the produced intermediate CHO^{*} is thermodynamically more favorable than COH^{*} over all examined surfaces (i.e., Cu(100), Cu(111), Pd₁Cu(100) and Pd₁Cu(111)) (Supplementary Fig. S23 and Tables S10–S13). The reasons that we followed the Langmuir-Hinshelwood (LH) mechanism (CO^{*} hydrogenates through a surface H^{*}) is that (1) Our ATR-SEIRAS results (Fig. 6, Supplementary Fig. S21, and Table S9) suggest a clearly more prominent CHO^{*} rather than COH^{*} as the C₁ intermediate over the Cu-based SAA surfaces when using KHCO₃ solution as the electrolyte and a previous theoretical study showed that CO hydrogenation tends to form CHO^{*} by the surface H^{*}⁴⁰, (2) The LH mechanism is also consistent with the kinetic order study of the electrochemical CORR-to-CH₄⁴¹ i.e.,

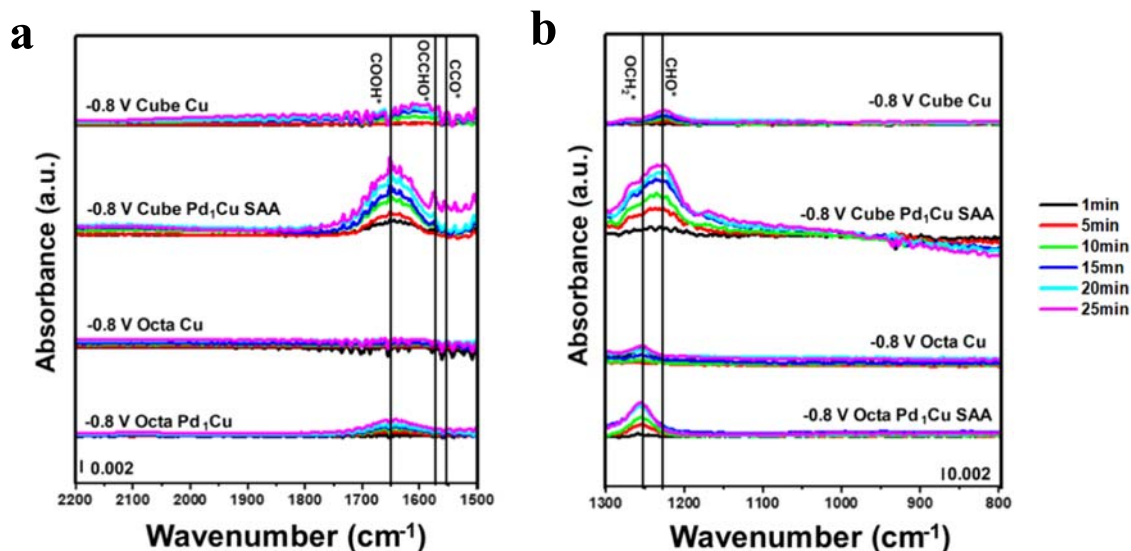


Fig. 6 | in-situ ATR-SEIRAS of shape-controlled Cu and Pd₁Cu SAA. The spectra **a** at higher wavenumbers and **b** at lower wavenumbers collected as a function of time for shape-controlled Pd₁Cu SAA and shape-controlled Cu in CO₂-saturated 0.5 M KHCO₃ electrolyte at -0.8 V. Spectra situated between 1300 and 1500 cm⁻¹ were omitted because of data distortions and overlaps caused by (b) carbonate species. For easier readability and format consistency, we put the * toward the end of the reaction intermediates in this report, and readers shall defer to the

computational models to determine the actual terminal atom for those adsorbates. To ensure that the study of the reaction mechanism by identification of intermediates using ATR-SEIRAS was not compromised by structural and morphological transformations of catalyst, we performed TEM and XRD analyses of cube-based samples as-prepared/post-reaction. The results summarized in Fig. S22 suggest that overall the catalysts are stable under the period of our ATR-SEIRAS test. (a.u.: arbitrary units).

the CO hydrogenation had a negative reaction order since CO* and H* are in competition with each other for surface sites and this does not agree with the Eley-Rideal (ER) mechanism, in which a positive reaction order in the partial pressure of CO should be expected.

We acknowledge that the intermediates involved in C-C coupling are still under debate. Some studies consider CO dimerization^{36,37}, while some other studies contemplate CO-CHO coupling^{42,43}. In this work, we followed CO-CHO coupling because we observed more abundant CHO* and OCCHO* species from the in-situ ATR-SEIRAS experiment for the Cube-series catalysts that favor ethylene formation. In addition, we performed DFT calculations to further confirm this C-C coupling process (i.e., CO dimerization, CO-CHO coupling) by comparing the reaction energy of both CO* + CHO* → OCCHO* + * and CO* + CO* → OCCO* + * (Supplementary Fig. S24). Our results show that CO-CHO coupling is more thermodynamically favorable than CO dimerization.

When the reactions are “forced” to occur on the single-atom Pd site of the clean Pd₁Cu SAA surfaces, the reaction free energies of CO* hydrogenation and C-C coupling decreases, but their activation barriers increase, compared to those steps over pure Cu (Fig. 7 and Supplementary Table S14). This indicates that although the single-atom Pd site within the SAA surface could favor the thermodynamic energies of the potential RDSs of CO₂RR to hydrocarbons, their kinetic properties could be inhibited since the corresponding activation barriers significantly increased. However, as a consequence of the Pd sites in Pd₁Cu SAA populating the surface with CO* (CO-Pd₁Cu(III)), both the reaction free energy and activation barriers of CO* hydrogenation to CHO* are 0.21 eV and 0.22 eV lower over the Cu sites of the CO-Pd₁Cu(III) catalyst compared to those over the Cu(III), respectively (Fig. 7a). We obtained similar results of C-C coupling over CO-Pd₁Cu(100) (Fig. 7b) which suggests that the CO* adsorption over the Pd site of SAA induces the surface lateral interaction and destabilizes the adsorption of the initial state (IS) of CO* hydrogenation and C-C coupling steps more than that of the transition state (TS) and final state (FS). Similar to the Pd₁Cu SAA, with a pre-existing CO* on the top of the Pt site of Pt₁Cu SAA, the reaction free energies of CO* hydrogenation

and C-C coupling over the Cu site of CO-Pt₁Cu SAA also become more thermodynamically favorable compared to those over the bare Cu catalysts (Supplementary Figs. S15 and S25). Taken together, this work paves the way for loading of atomically dispersed PGM atoms on single-crystal Cu surfaces in future endeavors, and we conclude that the promotion effect of single-atom PGM (i.e., Pd, Pt) on the Cu matrix on the CO₂RR can be promising.

Discussion

We adopted a wet chemical approach for synthesizing polycrystalline Cu NPs with a wide particle size distribution (50–150 nm range). The CO₂RR activity exhibited by our polycrystalline Cu NPs is thus lower than some of the engineered Cu materials tested in flow-cell configurations. These reported high performances were achieved by engineering copper catalysts to introduce grain boundaries as the new active sites^{44,45} or optimizing the catalyst layer at a device level through vacuum deposition techniques and catalyst-ionomer heterojunctions^{22,46–48}. As the overall reaction performance is sensitive to various factors beyond catalytic materials design, we acknowledge these above advancements, and we reiterate that this work focuses on tailoring PGM chemistry on metallic copper nanocatalysts (see XPS results in Supplementary Fig. S26). We caution readers that the multi-fold increase in partial current density for HCs reported for the polycrystalline Pd₁Cu SAA catalyst at -1.1 V *vs.* RHE using 0.5 M KHCO₃ electrolyte shall not be considered as absolute optimal performances, because tuning parameters such as catalyst loading, cell configuration, voltages, and electrolyte will further induce profound influences on the reaction performances. In addition, there are intertwined effects even during the reaction, where the more active SAA catalysts will indeed bring up the local pH and the higher local pH will further favor the targeted reaction. We were able to decouple these two impacts by showing that the alloying effect is major and the pH effect is minor (Supplementary Fig. S13b and associated discussion). Still, readers shall be cautious about how to interpret individual reactivity data, and the alloy *vs.* pH effects shall not be generalized.

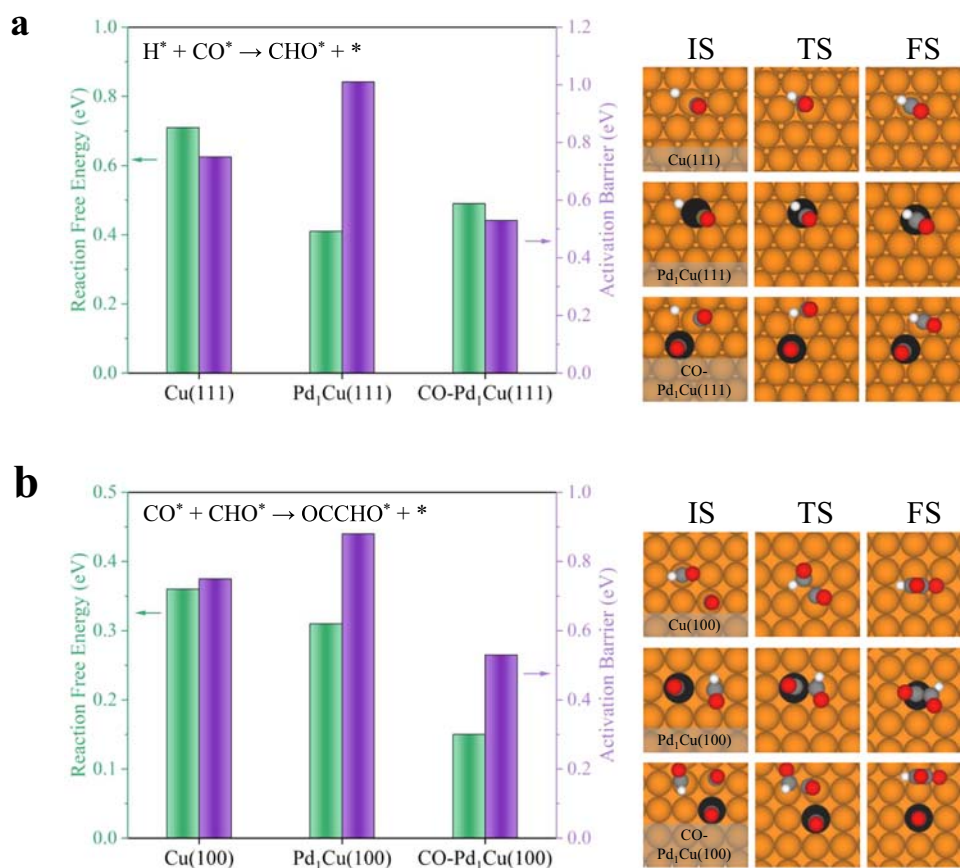


Fig. 7 | DFT calculations on the role of single-atom Pd in Pd₁Cu SAA on reaction free energy and activation barrier. **a** The reaction free energies and activation barriers of CO^{*} hydrogenation ($H^* + CO^* \rightarrow CHO^* + *$) on Cu(111), Pd₁Cu(111) and CO-Pd₁Cu(111) with the corresponding structures of IS, TS and FS. **b** The reaction free

energies and activation barriers of C-C coupling ($CO^* + CHO^* \rightarrow OCCHO^* + *$) on Cu(100), Pd₁Cu(100) and CO-Pd₁Cu(100) with the corresponding structures of IS, TS and FS. All the free energy and activation barrier were calculated at room temperature.

In line with a recent review by ref. ⁶, the secondary metals that show weaker H binding than Cu gain natural popularity in the established dilute Cu alloy research. We draw a corollary between our work and other exciting efforts of developing Cu-based alloys to display the merits. For example, Sn is generally believed to induce weaker H binding and stronger O binding than Cu in CO₂RR. As a consequence of varying Cu:Sn bulk compositions, the Sn-abundant surfaces have been shown to selectively produce formate, while the single-atom Sn on Cu favors CO formation^{10,49}. In another example, using single-atom Pb to alloy with Cu, Zheng et al. found that the Pb dopant regulated the Cu to preferentially adsorb HCOO^{*} over COOH^{*} during the CO₂RR and thus favored formate formation⁹. Perhaps due to the “co-introduction” synthesis approaches, a good portion of these metals were introduced to the bulk of the Cu. These secondary metal atoms throughout the surface and the bulk of the Cu host modified the catalytic property of Cu, and the obtained catalysts made products other than HCs. To that end, the goal of designing active and selective alloy catalysts for making deeply hydrogenated HCs products remains elusive⁵⁰. The Pd₁Cu and Pt₁Cu SAAs developed in this work, unexpectedly, would not agitate the HER reaction, but significantly promote the selective HCs formation in connection with respective facet control of the Cu hosts. On the better understood thermal catalytic system, the original concept of single-atom alloy catalysis was launched by Sykes and Stephanopoulos groups almost a decade ago^{51–53}, where the PGM₁Cu allows facile activation of incoming H₂ on the PGM site and enables the selective hydrogenation on Cu surfaces. Now, the weak or largely absent proof⁵⁴ of the exact single-atom alloy concept in electrocatalytic hydrogenation

has been identified and extended (e.g., HER mitigation and tunable host metal effects).

We also acknowledge the recent reports showing that perhaps the most effective catalytic centers for CO₂RR by Cu catalysts reside on the interfaces of different facets, edges, or corner sites of truncated nanoparticles^{55,56}. By anchoring PGMs exclusively at these specific locations instead of the entire surfaces as we did in this study, one may achieve intriguing reaction performances by using even less amount of PGMs in the interest of cost reduction. However, the present experimental and theoretical work designs were not intended for speculated site-specific PGM-Cu systems. Understanding precisely how the site-specific PGM-Cu chemistry will behave in the alternative but the related platform is worth a detailed study underway. The synthesis procedure adopted by us has the possibility of introducing other metal dopants and modifications of structures (both atomically and morphologically surface restructuring). While these factors are crucial, our studies on shape-controlled Cu-only and SAA catalysts suggest the overall reliability of our results in focusing on the PGM-Cu chemistry. A strong indication is that our shape-selective nanocatalysts displaying predominantly (111) and (100) facets delivered reaction selectivity agreeing well with the previously obtained selectivity results with cubes and octahedra for CO₂RR in literature^{31,57,58}.

Although it is out of the scope of the present work, we believe systematic single crystal studies originating from vacuum to model reactions (with operando pump-probe IR or Raman) would offer the best chance to avoid data noises (due to defects and impurities) and to interrogate the detailed reaction kinetics, mechanism, and the possible influence of atomic structure rearrangement caused by the galvanic

exchange between Pd and Cu. In the meantime, well-defined Cu surfaces and crystals may undergo surface structural changes during the CO₂RR reaction within a relatively brief time (e.g., a few hours)^{59,60}. Such a risk factor must be carefully considered and mitigated for detailed surface science studies. In the future, to gain a deeper understanding of the single-atom PGM effect on CO₂RR, we aim to develop a multi-scale, multi-physics simulation that quantitatively considers the electrode potential, pH, intermediate, and alloy effects.

We show in this work that platinum group metals, albeit being traditionally unfavored for electrocatalytic CO₂ hydrogenation, can now be leveraged as alloyed single atoms on the Cu matrix to dramatically improve the reaction efficiency to selectively produce hydrocarbon molecules, which is a reaction target that many other Cu-based alloys won't be able to achieve. With the PGM-heavy automotive catalysts phasing out under the megatrend of vehicle electrification, this newly found application of PGM catalysis unfolds unique opportunities for the global PGM market and workforce.

Methods

Cu Nanoparticles

We prepared polycrystalline Copper nanoparticles by wet chemical synthesis method using ascorbic acid (AA) and ethylene glycol (EG). AA acts as both a reducing agent as well an antioxidant. Thus, during the synthesis process, it avoids the formation of Cu oxides. AA can scavenge the free radicals and the dissolved oxygen in the reaction mixture giving it dual functionality. Typically, 319 mg of CuSO₄ (2 mmol) was dissolved in 100 mL ethylene glycol under vigorous stirring in the N₂ atmosphere. We maintained the temperature of the solution at 80 °C. 275 mg (2.5 mmol) of Polyvinylpyrrolidone (PVP-40K) was added to this and continued to stir until a clear solution. Separately, we dissolved 2.5 mmol of PVP and 2.8 g (16 mmol) of Ascorbic acid in 100 mL of EG until a clear solution. We prepared both solutions under a nitrogen atmosphere and vigorous stirring at 80 °C. The two solutions were mixed and allowed to react for 30 mins. 2 mmol of NaBH₄ was added to the final dispersion to reduce the unreacted Cu²⁺ to form 50–150 nm nanoparticles. The solution was collected in 50 mL tubes and centrifuged at 11,627 × *g* for 20 min. The Cu nanoparticles were washed with deionized water and ethanol three times each to obtain PVP-free Cu nanoparticles.

Cu shapes

We used the solvothermal method to synthesize the facet selective Cu nanoparticles.

Cubes. 21 mL of oleyl amine (OLAM) was degassed under vacuum until bubbling of dissolved gases stopped. We increased the temperature to 80 °C and switched the gas flow to N₂ to maintain the inert atmosphere. 430 mg (3 mmol) of CuBr was added and vigorously stirred until dissolved under N₂ flow. We added 1.16 g (3 mmol) of trioctylphosphine oxide (TOPO) and allowed it to dissolve. The temperature was then increased to 260 °C, keeping the inert atmosphere intact. The reaction was allowed for 2 h at 260 °C to form 50–120 nm nanoparticles, after which we cooled it with compressed gas. The resulting solution was quickly transferred to tubes and centrifuged at 11,627 × *g* for 20 min. We washed the product with hexane three times and re-dispersed it in O₂-free hexane for storage.

Octahedra. 48 mL of OLAM was degassed under vacuum until a gas bubble stopped appearing to remove dissolved gasses. We switched the Schlenk line to N₂ gas flow and increased the temperature to 80 °C. After 2 h, we increased the temperature to 335 °C. Separately and simultaneously, 395 mg of CuCl (4 mmol) and 1.78 mL (4 mmol) of Trioctyl phosphine (TOP) were heated to 200 °C under N₂ for 2 h to form the TOP-Cu complex. This complex was quickly and carefully added to hot OLAM and allowed to react for 30 min to form 40–200 nm

nanoparticles. We cooled the mixture under compressed air flow and promptly collected the product in tubes. They were centrifuged at 11,627 × *g* for 20 min and then washed three times with Toluene. Finally, we stored the Cu octahedra in O₂-free toluene for future use.

Galvanic displacement for SAA preparations

We performed rigorous initial optimizations by varying concentration, time, and reaction conditions to obtain homogeneously dispersed PGM metals on Cu Surface.

Pd₁Cu SAA. We prepared 50 mM H₂PdCl₄ by dissolving the 1:2 ratio of PdCl₂ and Conc. HCl at 60 °C. For the galvanic displacement, 30 mg of Cu nanoparticle was dispersed in 10 mL DI water under N₂ protection. We added 60 μL of the stock H₂PdCl₄ (50 mM) to the dispersion and stirred the mixture for 30 min under N₂ atmosphere. The final concentration of Pd used was 0.3 mM in the dispersion. After the reaction, the dispersion was centrifuged at 10k rpm for 20 min and washed with ethanol. We collected the first supernatant liquid for elemental analysis. The resulting powder after centrifugation is the Pd₁Cu SAA. We used the same procedure to obtain SAA of facet selective Cu morphology (cubes and octahedra).

Pt₁Cu SAA. We dispersed 30 mg of Cu nanoparticle in 10 mL of DI water under N₂ atmosphere. An aqueous solution of tetraamine Platinum (II) Nitrate [Pt(NH₃)₄(NO₃)₂] was added to this so that the total concentration of Pt²⁺ is 0.3 mM. We stirred the dispersion for 30 min under N₂ flow. The product was collected by centrifugation and washing with ethanol. We also collected the supernatant for elemental analysis.

PGMCu BA (M= Pd, Pt) bimetallic cluster alloys. We synthesized these sets of samples by wet chemical reduction instead of galvanic displacement reaction. 75 mg (0.47 mmol) of CuSO₄ was dissolved in 10 mL DI water, and we added aqueous solutions of H₂PdCl₄ or Pt(NH₃)₄(NO₃)₂ to keep the total concentration of Pd²⁺ or Pt²⁺ at 0.3 mM under stirring in the N₂ atmosphere. Then, we added 75 mg (2 mmol) of NaBH₄ to reduce the metal ions and form nanoparticles. The product was collected by centrifugation using the procedure mentioned above. For varied M (Pt and Pd): Cu ratios, we used different amounts of metal salts in the process. Among the various BA catalysts (Supplementary Table S1), the bimetallic alloy closely resembling the concentration of PGM in the SAA catalyst was used to compare the CO₂ reduction activity in the main text.

Morphology and composition study

The elemental composition of obtained samples was analyzed using ICP-OES (Thermo Fisher iCAP 7200 ICP-OES Analyzer) and Energy Dispersion X-ray Spectroscopy (EDS). XRD patterns were collected using an X-ray diffractometer (Rigaku D/max 2500) at a scan rate of 1° min⁻¹ in the 2θ range of 10–70°. We recorded the Field emission scanning electron microscopy (FE-SEM) images using a Hitachi SU9000 CFE SEM/STEM with a resolution of 0.4 nm at 30 kV (SE). We obtained TEM images and SAED patterns using the Hitachi HT7830 UHR 120 kV instrument with a resolution of 0.14 nm. We recorded Atomic-resolution aberration-corrected HAADF-STEM images and EDS mappings using JEOL JEM-ARM2100F equipped with a CEOS probe corrector. Preliminary We collected XAS data at Beamline 12-BM, Argonne National Laboratory (APS); Pd K-edge absorption spectra were acquired using a water-cooled double Si (311) monochromator. We recorded the spectra in the fluorescence mode with a 7-element silicon drift detector (SDD, Vortex ME-7, Hitachi). For the EXAFS analysis of samples after electrochemical reaction, catalyst coated GDLC were treated under typical CO₂RR reaction conditions (0.5 M KHCO₃ as an electrolyte and at -1.1 V (vs. RHE)) for 30 min. BF-STEM images of the post-reaction sample were acquired in the Center for Nanophase

Materials Sciences (CNMS) at Oak Ridge National Laboratory (ORNL) on a Nion UltraSTEM 100. The instrument was operated at 60 kV with a semiconvergence angle of -31 mrad.

Electrochemical measurements

We performed all electrocatalytic CO₂ reduction, and in-situ ATR-SEIRAS experiments on a CHI 760E workstation. For the initial investigations, a custom-built 60 mL two-compartment H-cell was used with a Sustainion membrane (Dioxide Materials) as the separating membrane between the counter and working electrode compartment. We fabricated the working electrode by drop-drying 200 μ L of catalyst dispersion (30 mg in 3 mL ethanol) on a pre-wet (with ethanol) gas diffusion electrode (Sigracet 39BB) with loading at ca. 200–250 μ g/cm². We studied the CO₂RR activity of the samples in a continuous flow cell reactor with Pt (1 cm²) foil as counter and Ag/AgCl (sat. KCl) as reference electrode. We maintained the total feed gas flow was at 23 sccm and the electrolyte circulation flow rate was 4 mL/min. The flow rate reported here is the gas flow rate at the cell outlet. The flow rates from the reactor outlet are almost identical ($< \pm 5\%$, within the error of MFCs) to the inlet flow rates set by the mass flow meters. Therefore, we did not apply flow rate corrections when using KHCO₃ solution as the electrolyte^{61,62}. However, we caution that this approximation cannot be universally applied, where the accumulative impact of CO₂ loss, reaction stoichiometry governed volume change, and overall conversion could become significant even when the inlet and outlet gas flow temperatures are the same. Thus, the flow rate correction becomes a must in such a case. Flow rate corrections became necessary for alternative tests where the KOH electrolyte has been used as CO₂ loss was significant. The geometric dimension of the active area of the working electrode is 1 cm². Before electrochemical measurements, the whole reactor line was purged with Ar for 30 min and then with CO₂ for 30 min to saturate the system with CO₂. The open-circuit voltage was allowed to stabilize under these conditions. The outlet of the gas purging line was directed to a gas trap glassware and subsequently to an online mass spectrometer for gas product quantifications. The liquid products were quantified by collecting the electrolyte aliquots at different time intervals from catholyte flow and analyzed by ¹D ¹H NMR applying the water gate suppression technique (using DMSO as the internal standard). We calculated the Faradaic efficiency using the Eq. (1) as follows:

$$\text{Faradaic Efficiency}(\%) = \frac{\text{moles of product} \times n \times F}{I \times t} \quad (1)$$

Where n is the number of electrons required to form product from CO₂ reduction in a balanced chemical equation (for example, $n = 2$ for CO, H₂, $n = 8$ for CH₄, etc.). F is the Faraday constant (96,485 C). I and t are the current and time from electrochemical biasing of working electrodes at different voltages. Potential is a reference to reversible hydrogen electrode by converting Ag/AgCl using Nernst equation as Eq. (2):

$$E(\text{RHE}) = E(\text{Ag}/\text{AgCl}) + E^0(\text{Ag}/\text{AgCl}) + 0.059 \times \text{pH} \quad (2)$$

As a control experiment, we performed reaction tests with Ar-only gas feed stream, while keeping the rest of the setups the same. H₂ was the only product that we had detected in an appreciable amount (FE% over 95%, Supplementary Figs. S7 and S8). This validates that the hydrocarbon products during the CO₂RR originate from the gaseous CO₂ feed stream. For the EXAFS analysis of samples after the electrochemical reaction, catalyst-coated GDL were treated under typical CO₂RR reaction conditions (0.5 M KHCO₃ as an electrolyte and at -1.1 V (vs. RHE)) for 30 min. The Faradaic efficiency reported here is within the error range of $\pm 5\%$.

CO Stripping experiment

The CO stripping was performed by potentiostatically adsorbing the CO monolayer on the catalyst's surface. 0.1 M H₂SO₄ was used as electrolyte to simultaneously monitor hydrogen underpotential deposition (H_{UPD}) and CO adsorption. We performed the experiments using the catalyst deposited on the gas diffusion electrode. The electrolyte was purged with Argon for 30 min, and the catalyst surface was cleaned electrochemically by cyclic voltammetry between 0 V to 1 V (vs RHE). The electrode was then biased at 0.1 V (RHE) while purging CO gas (5% CO, balanced Ar) for 5 min to allow the adsorption of CO on the catalyst surface. After the potentiostatic adsorption, the electrolyte was re-purged with Ar to remove any dissolved CO in the electrolyte. We recorded the CV between 0 V and 1.3 V to observe any CO stripping peak and HUPD peaks in subsequent cycles.

in-situ ATR-SEIRAS

in-situ ATR-SEIRAS: We performed SEIRAS experiments in a custom-built J1 Jackfish SEC cell with a face-angled crystal (FAC) as the working electrode substrate. The setup is compatible with PIKE VeeMAX III variable angle ATR sampling as used in the Thermo Nicolet i550 FTIR instrument. First, a thin Au film was formed on the surface of Si FAC to prepare working electrodes. Then a catalyst ink was prepared by dispersing 10 mg of catalyst in 1 mL isopropanol, 50 μ L of 5 wt% Nafion solution and sonication for 30 mins. 20 μ L of this ink was drop-casted on the Au thin film-coated Si FAC surface and allowed to dry overnight. The experiments were performed in 60 mL airtight single chamber glassware with dedicated ports for gas bubblers, counter and reference electrodes, and exhaust traps. We used 0.5 M KHCO₃ as an electrolyte, and before experiments, it was purged with N₂ to remove any dissolved oxygen. We collected the baseline at -0.45 V, by saturating the electrolyte with CO₂. We used Pt coil and Ag/AgCl (Sat. KCl) as a counter and reference electrode. We averaged 32 scans with a resolution of 4 cm⁻¹ for the final SEIRAS data collection. The data was collected by biasing the working electrode at a specific voltage and recording the SEIRAS signal every 5 min (for 30 min) to see the peaks' evolution patterns as a time function. In the plotted data, spectra situated between 1300 and 1500 cm⁻¹ were omitted because of the reported and confirmed absorbance overlaps and distortions caused by (bi)carbonate species³⁶.

Computational details

We performed all density functional theory (DFT) calculations using Vienna Ab Initio Simulation Package (VASP) code. We applied the revised Perdew-Burke-Ernzerhof (RPBE) functional, and the projector augmented wave (PAW) method to treat exchange-correlation interactions in a periodic boundary system. We used the climbing image nudged elastic band (CI-NEB) and dimer methods to search for the transition state. For geometries considerations, we considered the configurations optimized when the energy had converged to 10⁻⁴ eV, and the forces were smaller than 0.03 eV/Å. We described the detailed theoretical approaches and results in the Supplementary Information.

Data availability

All data generated or analyzed during this study are included in this published article and its supplementary information files.

References

- Hori, Y. In *Modern Aspects of Electrochemistry* (eds C. G. Vayenas, R. E. White, & M. E. Gamboa-Aldeco) 89–189 (Springer, 2008).
- Bagger, A., Ju, W., Varela, A. S., Strasser, P. & Rossmeisl, J. Single site porphyrine-like structures advantages over metals for selective electrochemical CO₂ reduction. *Catal. Today* **288**, 74–78 (2017).
- Bagger, A., Ju, W., Varela, A. S., Strasser, P. & Rossmeisl, J. Electrochemical CO₂ reduction: a classification problem. *Chem-PhysChem* **18**, 3266–3273 (2017).

- Huang, J., Mensi, M., Oveisi, E., Mantella, V. & Buonsanti, R. Structural sensitivities in bimetallic catalysts for electrochemical CO₂ reduction revealed by Ag–Cu nanodimers. *J. Am. Chem. Soc.* **141**, 2490–2499 (2019).
- Li, Y. C. et al. Binding site diversity promotes CO₂ electroreduction to ethanol. *J. Am. Chem. Soc.* **141**, 8584–8591 (2019).
- Vasileff, A., Xu, C., Jiao, Y., Zheng, Y. & Qiao, S.-Z. Surface and interface engineering in copper-based bimetallic materials for selective CO₂ electroreduction. *Chem* **4**, 1809–1831 (2018).
- Kim, D. et al. Electrochemical activation of CO₂ through atomic ordering transformations of AuCu nanoparticles. *J. Am. Chem. Soc.* **139**, 8329–8336 (2017).
- Choi, J. et al. Electrochemical CO₂ reduction to CO on dendritic Ag–Cu electrocatalysts prepared by electrodeposition. *Chem. Eng. J.* **299**, 37–44 (2016).
- Zheng, T. et al. Copper-catalysed exclusive CO₂ to pure formic acid conversion via single-atom alloying. *Nat. Nanotechnol.* **16**, 1386–1393 (2021).
- Ren, W. et al. Isolated copper–tin atomic interfaces tuning electrocatalytic CO₂ conversion. *Nat. Commun.* **12**, 1449 (2021).
- Xie, H. et al. Weakening intermediate bindings on CuPd/Pd core/shell nanoparticles to achieve Pt-like bifunctional activity for hydrogen evolution and oxygen reduction reactions. *Adv. Funct. Mater.* **31**, 2100883 (2021).
- Varela, A. S. et al. CO₂ electroreduction on well-defined bimetallic surfaces: Cu overlayers on Pt(111) and Pt(211). *J. Phys. Chem. C* **117**, 20500–20508 (2013).
- Zhao, X., Luo, B., Long, R., Wang, C. & Xiong, Y. Composition-dependent activity of Cu–Pt alloy nanocubes for electrocatalytic CO₂ reduction. *J. Mater. Chem. A* **3**, 4134–4138 (2015).
- Mun, Y. et al. Cu–Pd alloy nanoparticles as highly selective catalysts for efficient electrochemical reduction of CO₂ to CO. *Appl. Catal. B Environ.* **246**, 82–88 (2019).
- Zhu, W. et al. Morphological and compositional design of Pd–Cu bimetallic nanocatalysts with controllable product selectivity toward CO₂ electroreduction. *Small* **14**, 1703314 (2018).
- Shi, C., Hansen, H. A., Lausche, A. C. & Nørskov, J. K. Trends in electrochemical CO₂ reduction activity for open and close-packed metal surfaces. *Phys. Chem. Chem. Phys.* **16**, 4720–4727 (2014).
- Li, J. et al. Constraining CO coverage on copper promotes high-efficiency ethylene electroproduction. *Nat. Catal.* **2**, 1124–1131 (2019).
- Schreier, M., Yoon, Y., Jackson, M. N. & Surendranath, Y. Competition between H and CO for active sites governs copper-mediated electrosynthesis of hydrocarbon fuels. *Angew. Chem. Int. Ed.* **57**, 10221–10225 (2018).
- Zhang, Y.-J., Sethuraman, V., Michalsky, R. & Peterson, A. A. Competition between CO₂ reduction and H₂ evolution on transition-metal electrocatalysts. *ACS Catal.* **4**, 3742–3748 (2014).
- Cave, E. R. et al. Trends in the catalytic activity of hydrogen evolution during CO₂ electroreduction on transition metals. *ACS Catal.* **8**, 3035–3040 (2018).
- Hansen, J. N. et al. Is there anything better than Pt for HER? *ACS Energy Lett.* **6**, 1175–1180 (2021).
- Arquer, F. P. G. D. et al. CO₂ electrolysis to multicarbon products at activities greater than 1 A cm². *Science* **367**, 661–666 (2020).
- Xie, Y. et al. High carbon utilization in CO₂ reduction to multi-carbon products in acidic media. *Nat. Catal.* **5**, 564–570 (2022).
- Wang, X. et al. Gold-in-copper at low *CO coverage enables efficient electromethanation of CO₂. *Nat. Commun.* **12**, 3387 (2021).
- Yu, W., Xie, H., Chen, L., Li, Y. & Zhang, C. Synthesis and Characterization of Monodispersed Copper Colloids in Polar Solvents. *Nanoscale Res. Lett.* **4**, 465 (2009).
- Xiong, J., Wang, Y., Xue, Q. & Wu, X. Synthesis of highly stable dispersions of nanosized copper particles using l-ascorbic acid. *Green. Chem.* **13**, 900–904 (2011).
- Li, J. et al. Enhanced multi-carbon alcohol electroproduction from CO via modulated hydrogen adsorption. *Nat. Commun.* **11**, 3685 (2020).
- Pei, G. X. et al. Performance of Cu-Alloyed Pd single-atom catalyst for semihydrogenation of acetylene under simulated front-end conditions. *ACS Catal.* **7**, 1491–1500 (2017).
- Xing, F., Jeon, J., Toyao, T., Shimizu, K.-I. & Furukawa, S. A Cu–Pd single-atom alloy catalyst for highly efficient NO reduction. *Chem. Sci.* **10**, 8292–8298 (2019).
- Nilsson, J., Carlsson, P.-A., Grönbeck, H. & Skoglundh, M. First principles calculations of palladium nanoparticle XANES spectra. *Top. Catal.* **60**, 283–288 (2017).
- Rossi, K. & Buonsanti, R. Shaping copper nanocatalysts to steer selectivity in the electrochemical CO₂ reduction reaction. *Acc. Chem. Res.* **55**, 629–637 (2022).
- Louidice, A. et al. Tailoring copper nanocrystals towards C₂ products in electrochemical CO₂ reduction. *Angew. Chem. Int. Ed.* **55**, 5789–5792 (2016).
- Reske, R., Mistry, H., Behafarid, F., Roldan Cuenya, B. & Strasser, P. Particle size effects in the catalytic electroreduction of CO₂ on Cu nanoparticles. *J. Am. Chem. Soc.* **136**, 6978–6986 (2014).
- Gunathunge, C. M. et al. Spectroscopic observation of reversible surface reconstruction of copper electrodes under CO₂ reduction. *J. Phys. Chem. C* **121**, 12337–12344 (2017).
- Zhu, S., Jiang, B., Cai, W.-B. & Shao, M. Direct observation on reaction intermediates and the role of bicarbonate anions in CO₂ electrochemical reduction reaction on Cu surfaces. *J. Am. Chem. Soc.* **139**, 15664–15667 (2017).
- Kim, Y. et al. Time-resolved observation of C–C coupling intermediates on Cu electrodes for selective electrochemical CO₂ reduction. *Energy Environ. Sci.* **13**, 4301–4311 (2020).
- Pérez-Gallent, E. et al. Spectroscopic observation of a hydrogenated CO dimer intermediate during CO reduction on Cu (100) electrodes. *Angew. Chem.* **129**, 3675–3678 (2017).
- Han, L. et al. Stable and efficient single-atom Zn catalyst for CO₂ reduction to CH₄. *J. Am. Chem. Soc.* **142**, 12563–12567 (2020).
- Nitopi, S. et al. Progress and perspectives of electrochemical CO₂ reduction on copper in aqueous electrolyte. *Chem. Rev.* **119**, 7610–7672 (2019).
- Hussain, J., Jónsson, H. & Skúlason, E. Calculations of product selectivity in electrochemical CO₂ reduction. *ACS Catal.* **8**, 5240–5249 (2018).
- Schreier, M. et al. Competition between H and CO for active sites governs copper-mediated electrosynthesis of hydrocarbon fuels. *Angew. Chem.* **130**, 10378–10382 (2018).
- Goodpaster, J. D., Bell, A. T. & Head-Gordon, M. Identification of possible pathways for C–C bond formation during electrochemical reduction of CO₂: new theoretical insights from an improved electrochemical model. *J. Phys. Chem. Lett.* **7**, 1471–1477 (2016).
- Garza, A. J., Bell, A. T. & Head-Gordon, M. Mechanism of CO₂ reduction at copper surfaces: pathways to C₂ products. *ACS Catal.* **8**, 1490–1499 (2018).
- Jiang, K. et al. Metal ion cycling of Cu foil for selective C–C coupling in electrochemical CO₂ reduction. *Nat. Catal.* **1**, 111–119 (2018).
- Li, C. W., Ciston, J. & Kanan, M. W. Electroreduction of carbon monoxide to liquid fuel on oxide-derived nanocrystalline copper. *Nature* **508**, 504–507 (2014).
- Zhang, G. et al. Efficient CO₂ electroreduction on facet-selective copper films with high conversion rate. *Nat. Commun.* **12**, 1–11 (2021).

47. Zhang, Z. et al. Tailoring the surface and interface structures of copper-based catalysts for electrochemical reduction of CO₂ to ethylene and ethanol. *Small* **18**, 2107450 (2022).
48. Yu, J. et al. Recent progresses in electrochemical carbon dioxide reduction on copper-based catalysts toward multicarbon products. *Adv. Funct. Mater.* **31**, 2102151 (2021).
49. Zhang, M. et al. Tunable selectivity for electrochemical CO₂ reduction by bimetallic Cu–Sn catalysts: elucidating the roles of Cu and Sn. *ACS Catal.* **11**, 11103–11108 (2021).
50. Chernyshova, I. V., Somasundaran, P. & Ponnurangam, S. On the origin of the elusive first intermediate of CO₂ electroreduction. *Proc. Natl Acad. Sci. USA* **115**, E9261–E9270 (2018).
51. Kyriakou, G. et al. Isolated metal atom geometries as a strategy for selective heterogeneous hydrogenations. *Science* **335**, 1209–1212 (2012).
52. Lucci, F. R. et al. Selective hydrogenation of 1,3-butadiene on platinum–copper alloys at the single-atom limit. *Nat. Commun.* **6**, 8550 (2015).
53. Liu, J. et al. Tackling CO poisoning with single-atom alloy catalysts. *J. Am. Chem. Soc.* **138**, 6396–6399 (2016).
54. Hannagan, R. T., Giannakakis, G., Flytzani-Stephanopoulos, M. & Sykes, E. C. H. Single-atom alloy catalysis. *Chem. Rev.* **120**, 12044–12088 (2020).
55. Hagman, B. et al. Steps control the dissociation of CO₂ on Cu(100). *J. Am. Chem. Soc.* **140**, 12974–12979 (2018).
56. Cheng, D. et al. The nature of active sites for carbon dioxide electroreduction over oxide-derived copper catalysts. *Nat. Commun.* **12**, 395 (2021).
57. Zhang, G. et al. Efficient CO₂ electroreduction on facet-selective copper films with high conversion rate. *Nat. Commun.* **12**, 5745 (2021).
58. Liu, X. et al. Understanding trends in electrochemical carbon dioxide reduction rates. *Nat. Commun.* **8**, 15438 (2017).
59. Simon, G. H. et al. Potential-dependent morphology of copper catalysts during CO₂ electroreduction revealed by in situ atomic force microscopy. *Angew. Chem. Int. Ed.* **60**, 2561–2568 (2021).
60. Scholten, F. et al. Identifying structure–selectivity correlations in the electrochemical reduction of CO₂: A comparison of well-ordered atomically clean and chemically etched copper single-crystal. *Surf. Angew. Chem. Int. Ed.* **60**, 19169–19175 (2021).
61. Ren, D., Gao, J., Zakeeruddin, S. M. & Gratzel, M. New insights into the interface of electrochemical flow cells for carbon dioxide reduction to ethylene. *J. Phys. Chem. Lett.* **12**, 7583–7589 (2021).
62. Ma, M. et al. Insights into the carbon balance for CO₂ electroreduction on Cu using gas diffusion electrode reactor designs. *Energy Environ. Sci.* **13**, 977–985 (2020).

Acknowledgements

M.Y. thanks the support provided by the start-up fund and the Creative Inquiry Program (CI#2186) of Clemson University, NASA EPSCoR (SC-80NSSC22M020), and the use of 12-BM beamline of the Advanced Photon Source is supported by the U.S. Department of Energy (DOE) Office of Science User Facility operated for the DOE Office of Science by the Argonne National Laboratory under Contract No. DE-AC02-06CH11357. The Electron microscopy facility was supported by Drs. Laxmikant Saraf and Haijun Qian at Clemson University Electron Microscopy Facility. Instruments were supported by Dr. Rakesh Sachdeva at the Department of Chemistry at Clemson University. Post-reaction sample scanning transmission electron microscopy research was supported by the Center for Nanophase Materials Sciences (CNMS), which is a US Department of Energy, Office of Science User Facility at Oak Ridge National Laboratory. M.C. thanks Clemson University for postdoctoral research funding. Z.J. and M.Y. thanks for the support from Hitachi High-Tech, USA 2022 Fellowship, Creative Inquiry program of Clemson

University. F.C. thanks the support from the institutional faculty start-up funds from the University of Massachusetts Lowell and National Science Foundation for partial support (award #2103478). M.W. and F.C. acknowledge the computational resources provided by the Massachusetts Green High-Performance Computing Center (MGHPCC). M.W. and F.C. also acknowledge the Extreme Science and Engineering Discovery Environment (XSEDE) at Texas Advanced Computing Center (TACC) Dell/Intel Knights Landing, Skylake System (Stampede2) and San Diego Supercomputer Center Expense through allocation CHE200083 Renewal for the computational facility support. Yang Group would like to thank the entire Rachel Getman Group for the fun and constructive discussions of catalysis science that we had at those joint group meetings at Clemson. M.Y. wishes good friend Dr. Rachel the best in her new endeavor in Ohio.

Author contributions

M.Y. and F.C. supervised the project. M.C. and M.Y. designed the research. M.C., Z.J., J.Y., C.S., and C.R. carried out electrochemical measurements and materials characterizations. Z.J. and M.C. performed in-situ ATR-SEIRAS experiments. M.W. carried out DFT calculations and analyzed data. H.W. performed electron microscopy experiments. S.L. performed XAFS experiments. C.B. helped review experimental progress and directions. M.Z. performed BF-STEM of post-reaction samples. M.C., Z.J., M.W., F.C., and M.Y. co-wrote the paper. All authors discussed the results and contributed to the preparation of the manuscript.

Competing interests

The authors declare no competing interests.

Additional information

Supplementary information The online version contains supplementary material available at <https://doi.org/10.1038/s41467-023-38777-y>.

Correspondence and requests for materials should be addressed to Fanglin Che or Ming Yang.

Peer review information *Nature Communications* thanks Yanguang Li, John Flake, and the other, anonymous, reviewer(s) for their contribution to the peer review of this work.

Reprints and permissions information is available at <http://www.nature.com/reprints>

Publisher's note Springer Nature remains neutral with regard to jurisdictional claims in published maps and institutional affiliations.

Open Access This article is licensed under a Creative Commons Attribution 4.0 International License, which permits use, sharing, adaptation, distribution and reproduction in any medium or format, as long as you give appropriate credit to the original author(s) and the source, provide a link to the Creative Commons license, and indicate if changes were made. The images or other third party material in this article are included in the article's Creative Commons license, unless indicated otherwise in a credit line to the material. If material is not included in the article's Creative Commons license and your intended use is not permitted by statutory regulation or exceeds the permitted use, you will need to obtain permission directly from the copyright holder. To view a copy of this license, visit <http://creativecommons.org/licenses/by/4.0/>.

© The Author(s) 2023